

An Infrared Interferometer for Elastoplastic Crack-Tip Field Investigation of Homogeneous and Bimaterial Beams: A Study of Three-Dimensional Effects and J -Dominance

J. K. Sinha
Graduate Student

H. V. Tippur¹
Associate Professor,
htippur@eng.auburn.edu,
Mem. ASME

Department of Mechanical Engineering,
Auburn University,
202 Ross Hall,
Auburn, AL 36849-5341

An infrared interferometer capable of performing real-time full-field noncontacting deformation field measurements on optically rough surfaces is proposed as a tool for elastoplastic fracture mechanics investigations. The choice of the infrared wavelength allows interferometric measurements on fracture samples with little or no surface preparation and is more tolerant of the damage accumulation near the crack. The interferometer also bridges a sensitivity gap among existing techniques for out-of-plane deformation measurement. First, a rigorous Fourier optics analysis is provided for the interferometer and the range of surface roughness that can be studied using this interferometer is examined. The interferometer is then used for mapping deformations near elastoplastically deformed cracks in aluminum beams and solder-copper bimaterials. The regions of dominant three-dimensional effects and J -dominance are examined on the sample surface by evaluating measurements along with companion finite element analyses and the HRR fields.

1 Introduction

Currently there is a need for optical techniques with full-field real-time noncontact measurement capabilities preferably with little or no surface preparation. Most engineering material surfaces are "optically rough" (relative to the visible wavelength of light) and need elaborate surface preparation—polishing/thin film deposition to obtain a specular surface, printing gratings, etc.—prior to real-time metrology using visible wavelengths. Also, when damage accumulates, as in the case with the onset of plasticity, surface textural changes increase the roughness rendering visible light interferograms unclear or result in peeling of thin film deposition. For example, the deformation field near an elastoplastically deformed notch in an aluminum beam studied using the Coherent Gradient Sensor (CGS) (Tippur et al., 1991) is shown in Fig. 1. The sample surface was made specularly reflective through a series of processes consisting of lapping, polishing, and thin film deposition prior to measurements. With the onset of plasticity, clearly, the discernability of fringes near the notch tip is affected even when plasticity effects are relatively small (plastic zone size (r_p) 0.6 times the plate thickness). On the other hand, there are several optical methods—holography, laser speckle interferometry, shearography to name a few—that are capable of performing measurements on rough surfaces. However, they involve double-exposure (one of which is a reference exposure) schemes

and hence do not offer real-time capability essential for many applications. Furthermore, surface textural changes and/or large deformations lead to speckle decorrelation effects resulting in a loss of fringe information and hence generally limited to elastic investigations.

A potential method of dealing with optically rough surfaces for real-time interferometric purposes is based on the theory of scattering of light by rough surfaces (Beckmann and Spizzichino, 1963). It is shown that the specular component of the scattered field increases with increasing wavelength for a randomly rough surface. Munnerlyn and Latta (1968) used mid-infrared radiation to relate fringe contrast and surface roughness based on average intensity measurement of an optical component in their studies. Optical component testing along with some quantitative insight into the influence of roughness of fringe contrast in the mid-infrared range of 10.6 μm is reported by Kwon et al. (1980). Recently, Lewandowski et al. (1989) have demonstrated infrared holographic interferometry facilitating fringe interpretations for large object displacements and minimizing the handicaps of visible holography. Persson (1993) has performed roughness measurement of machined surfaces using the speckle technique and has suggested that the measurement range could be extended if the experiments are performed in the infrared range.

In this paper an *infrared* Twyman-Green interferometer (wavelength 10.6 μm) has been developed as a new tool for elastoplastic crack-tip field mapping through rough surface measurements. The interferometer has real-time, full-field, and non-contact measurement capabilities. The textural changes and other surface roughness limitations commonly encountered when using visible radiation has been successfully overcome by a favorable roughness-to-wavelength ratio using infrared wavelengths. This offers greater flexibility in dealing with material surfaces in "as-is" conditions to perform real-time measurements. Furthermore, the measurement sensitivity offered by

¹ To whom correspondence should be addressed.

Contributed by the Applied Mechanics Division of THE AMERICAN SOCIETY OF MECHANICAL ENGINEERS for publication in the ASME JOURNAL OF APPLIED MECHANICS.

Discussion on the paper should be addressed to the Technical Editor, Professor Lewis T. Wheeler, Department of Mechanical Engineering, University of Houston, Houston, TX 77204-4792, and will be accepted until four months after final publication of the paper itself in the ASME JOURNAL OF APPLIED MECHANICS.

Manuscript received by the ASME Applied Mechanics Division, July 30, 1997; final revision, Jan. 16, 1998. Associate Technical Editor: I. M. Daniel.

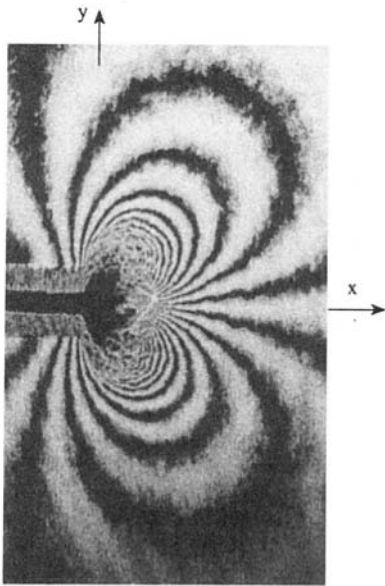


Fig. 1 Visible light interference patterns (contours of $\partial w/\partial y$) near an elastoplastically deformed notch in Al 6061 (Tippur et al., 1991); (plastic zone size ~ 0.6 times the plate thickness)

the proposed interferometer ($\sim 2.5 \mu\text{m}/\text{half-fringe}$) bridges a large gap in the measurement sensitivities among existing methods of shadow and projection moiré methods ($\sim 15\text{--}25 \mu\text{m}/\text{half-fringe}$) and visible light Twyman-Green interferometer ($\sim 0.3 \mu\text{m}/\text{half-fringe}$). A rigorous Fourier optics analysis based on the Fresnel approximation and randomly rough surfaces is provided. Based on the result, the tolerable range of surface roughness by the interferometer is first investigated. Next, the proposed interferometer's capabilities for out-of-plane displacement field mapping near elastoplastically deformed cracks in homogenous and bimaterial fracture specimens is demonstrated. The measurements have been used for identifying the region of dominant three-dimensional deformations in homogeneous beam specimens and for evaluating the J -integral. Corresponding regions of three-dimensional effects and first experimental evidence of a HRR-like region near an elastoplastically deformed interfacial crack in a solder-copper bimaterial beam are provided.

2 Twyman-Green Interferometer: Optical Setup

The optical set-up for the infrared Twyman-Green interferometer is shown in Fig. 2. It consists of a CO_2 laser, lenses— L_1 , L_2 , and L_3 , beamsplitters—BS1 and BS2, a reference mirror

and a pyroviewer camera connected to a TV monitor, and a hard copy unit. The object to be investigated is a typical "rough" surface encountered in engineering. The optical interference is a result of the path difference between the reference and test paths as shown.

A water-cooled Invar stabilized CO_2 laser operating at $10.6 \mu\text{m}$ wavelength with continuous 7.5 W output power was used as a coherent light source. The unexpanded laser beam is 3.5 mm in diameter and is vertically polarized. A universal controller is used for general purpose interface between the user signal and CO_2 laser adding flexibility of power output control. The experiments reported in this paper have been conducted with low-power levels of approximately five percent of the nominal power of the laser. Two ZnSe lenses L_1 and L_2 were used to expand the laser beam to approximately 35-mm beam diameter. All lenses used were the meniscus type to minimize spherical aberrations. A ZnSe (50/50) beamsplitter was used to split the beam into two components as shown in Fig. 2. The optical coatings are the dielectric type and are optimized for $10.6 \mu\text{m}$ wavelength and $45 \text{ deg} \pm 2$ percent incidence. The reference mirror is an aluminum-coated first-surface mirror. A Pyroviewer camera is used for imaging the interference fringes. This camera is designed to detect radiation in the $8\text{--}14 \mu\text{m}$ region. The recommended power threshold to prevent damage to the camera detector is $1 \text{ mW}/\text{cm}^2$. This being a rather small power, further reduction in the light intensity entering the optical set-up is accomplished by a 80/20 ZnSe beam splitter (BS2) that reflects away 80 percent of the incident energy as shown in Fig. 2.

3 Interference Analysis

Object surfaces encountered in engineering practice are generally "optically rough" and the differences are only in the degree and the type of roughness. Identifying the degree of roughness depends on both the geometry and the wavelength of the incident probe and is taken advantage of in this work. The types of roughness are generally classified into periodic roughness as in the case of machined surfaces and nonperiodic roughness, such as the random roughness of a sandblast surface. When a surface is illuminated with coherent light, the surface roughness and the orientation of the surface determine the general scattering pattern. As the surface roughness increases, the surface is perceived as changing from being smooth or specular to rough or diffuse. As the surface roughness increases the specular component of light decreases and the diffused light component increases. Thus specular reflection can be used as a measure of surface roughness. Rayleigh criterion characterizes the smoothness of a surface in terms of a parameter $\epsilon_R = (4\pi h/\lambda) \cos \theta_i$ ($\epsilon_R \ll 1$) where h is the surface peak amplitude, λ is wavelength of the incident light, and θ_i is the incident angle. Evidently, there are two ways of reducing ϵ_R : (i) by increasing

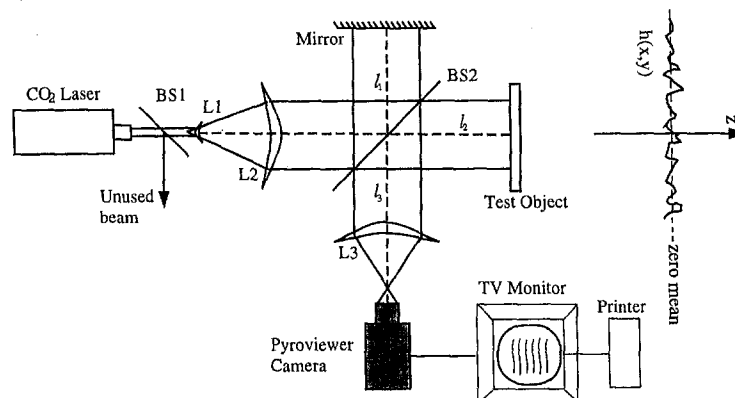


Fig. 2 Optical set-up for the Infrared Twyman-Green Interferometer

θ_i , and (ii) by increasing the wavelength (λ) of the incident light. Because the wavelength increase could be over an order of magnitude from the mid-visible to mid-infrared range and cosine function decreases when θ_i varies from 0–90 deg, it should be possible to extend the measurement techniques to surfaces that are traditionally considered far from being optically smooth.

In this work, the wavelength of light was increased in a Twyman-Green interferometer ($\theta_i = 0$) to perform out-of-plane deformation measurements on machined or natural surfaces. First, a study of the discernability of interference patterns in situations involving different surface roughness to test the feasibility of using infrared interferometry was performed. The fringe visibility and fringe contrast data were used to quantify operational limits of this interferometer in dealing with “rough” surfaces.

In the following a rigorous Fourier optics analysis of the interferometer that takes into account random surface roughness of the object is offered. The propagation of electromagnetic waves through the optical elements of the interferometer and the formation of interference patterns are systematically described by incorporating Fresnel diffraction principle based on the scalar theory of diffraction. The propagation of light waves from the j th plane to the $(j + 1)$ th plane located parallel to and at a distance z can be described as (Iizuka, 1985)

$$\begin{aligned} E_{j+1}(x_{j+1}, y_{j+1}) &= \frac{1}{i\lambda z} \exp\left(ik\left[z + \frac{x_{j+1}^2 + y_{j+1}^2}{2z}\right]\right) \mathfrak{S}\{E_j(x_j, y_j)g(x_j, y_j)\}, \\ &\equiv \frac{1}{i\lambda z} \exp\left(ik\left[z + \frac{x_{j+1}^2 + y_{j+1}^2}{2z}\right]\right) \\ &\times \int_{-\infty}^{\infty} \int_{-\infty}^{\infty} E_j(x_j, y_j) \exp\left(ik \frac{x_j^2 + y_j^2}{2z}\right) \\ &\times \exp\left(-\frac{ik}{z}\{x_j x_{j+1} + y_j y_{j+1}\}\right) dx_j dy_j, \quad (1) \end{aligned}$$

where E represents the complex amplitudes on the respective planes, $i = \sqrt{-1}$, $g(x_j, y_j)$ is the point-source transfer function $g(x_j, y_j) = A \exp(ik((x_j^2 + y_j^2)/2z))$ and $k (=2\pi/\lambda)$ is the wave number with λ the wavelength of the light. In the above, $\mathfrak{S}(\cdot)$ denotes the two-dimensional Fourier transform operator. The positive quadratic phase term represents spherical waves emanating (diverging) from the current wave front to the next based on Huygens' principle which idealizes the wave front as a conglomeration of point sources.

Now, consider a plane wave incident on the object surface (x_o, y_o) and a planar reference mirror (x_r, y_r) as shown in Fig. 3. After reflecting from the object and the reference surfaces,

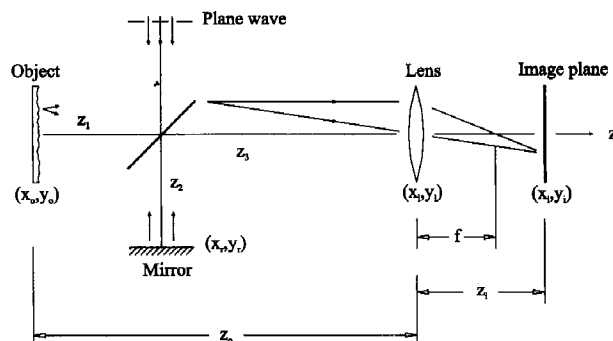


Fig. 3 Schematic of the interferometer used in the interference analysis

the waves propagate to the imaging lens located at the plane denoted by (x_l, y_l) . Using Eq. (1) and letting $z_1 + z_3 = z_o$ and $z_1 + z_2 = z_r$, the complex amplitude distribution E_l^- , just before the lens plane, can be expressed as

$$\begin{aligned} E_l^-(x_l, y_l) &= \frac{A_o}{i\lambda z_o} \exp\left(ik\left[z_o + \frac{x_l^2 + y_l^2}{2z_o}\right]\right) \\ &\times \mathfrak{S}\left\{E_o(x_o, y_o) \exp\left(ik \frac{x_o^2 + y_o^2}{2z_o}\right)\right\} \\ &+ \frac{A_r}{i\lambda z_r} \exp\left(ik\left[z_r + \frac{x_l^2 + y_l^2}{2z_r}\right]\right) \\ &\times \mathfrak{S}\left\{E_r(x_r, y_r) \exp\left(ik \frac{x_r^2 + y_r^2}{2z_r}\right)\right\}, \quad (2) \end{aligned}$$

where A_o and A_r denote the maximum amplitude of the object and reference waves upon reflection and $E_q(x_q, y_q)$ ($q = o, r, l, i$) denote the complex amplitude distributions on different planes. A thin spherical lens is a phase object which modulates the incident waves as

$$E_l^+(x_l, y_l) = E_l^-(x_l, y_l) \exp\left(ik\left[n_l \Delta_l - \frac{x_l^2 + y_l^2}{2f}\right]\right), \quad (3)$$

where E_l^+ is the amplitude distribution exiting the lens and the negative sign in front of the quadratic phase term represents converging spherical waves to the back focal point when a positive lens is used. In the above, Δ_l is the maximum thickness, n_l the refractive index, and f the focal length of the lens. Using Eqs. (1)–(3), the amplitude distribution on the image plane (x_i, y_i) of the recording lens can be expressed as

$$\begin{aligned} E_i(x_i, y_i) &= \frac{1}{i\lambda z_i} \exp\left(ik\left[n_l \Delta_l + z_i + \frac{x_i^2 + y_i^2}{2z_i}\right]\right) \\ &\times \mathfrak{S}\left\{E_l^-(x_l, y_l) \exp\left(ik\left[-\frac{x_l^2 + y_l^2}{2f} + \frac{x_i^2 + y_i^2}{2z_i}\right]\right)\right\}. \quad (4) \end{aligned}$$

Substituting for $E_l^-(x_l, y_l)$ from Eq. (2) in the above we get

$$\begin{aligned} E_i(x_i, y_i) &= \frac{1}{i\lambda z_i} \exp\left(ik\left[n_l \Delta_l + z_i + \frac{x_i^2 + y_i^2}{2z_i}\right]\right) \\ &\times \mathfrak{S}\left[\left(\frac{A_o}{i\lambda z_o} \exp\left(ik\left[z_o + \frac{x_l^2 + y_l^2}{2z_o}\right]\right)\right)\right. \\ &\times \mathfrak{S}\left\{E_o(x_o, y_o) \exp\left(ik \frac{x_o^2 + y_o^2}{2z_o}\right)\right\} \\ &+ \frac{A_r}{i\lambda z_r} \exp\left(ik\left[z_r + \frac{x_l^2 + y_l^2}{2z_r}\right]\right) \\ &\times \mathfrak{S}\left\{E_r(x_r, y_r) \exp\left(ik \frac{x_r^2 + y_r^2}{2z_r}\right)\right\} \\ &\left.\times \exp\left(ik\left[-\frac{x_l^2 + y_l^2}{2f} + \frac{x_i^2 + y_i^2}{2z_i}\right]\right)\right]. \quad (5) \end{aligned}$$

Thus far, for clarity the coordinates of the object plane and the reference plane are distinguished through the use of subscripts o and r , respectively. In reality, the two are interchangeable, ($x_r \equiv x_o$ and $y_r \equiv y_o$) thereby implying that radiation from a generic

point on the object surface interferes with a plane wave generated by a corresponding point on the mirror. Now, for an equal arm interferometer with $z_o = z_r$ and when the imaging system is focussed on the object plane, we get

$$E_i(x_i, y_i) = c \exp\left(ik\left\{n_l \Delta_l + z_i + \frac{x_i^2 + y_i^2}{2z_i} + z_o + \frac{x_o^2 + y_o^2}{2z_o}\right\}\right) \times \{A_o E_o(-x_o, -y_o) + A_r E_r(-x_r, -y_r)\}, \quad (6)$$

where the identity $\mathfrak{S}(\mathfrak{S}\{E(x)\}) = E(-x)$ and the lens equation $(1/z_o) + (1/z_i) - (1/f) = 0$, have been utilized and c is a constant. The constant c will be dropped in the rest of the analysis since it has no bearing on the final outcome. The negative signs in front of the Cartesian coordinates in Eq. (6) physically suggests the inversion of the image of the object on the image plane.

To further describe the amplitude and hence the intensity distribution on the image plane, E_o and E_r need to be more specific. In the present interferometer, E_r denotes the amplitude distribution from a plane mirror perpendicular to the optical axis and hence $E_r(x_r, y_r) = 1$. For an object surface with a randomly varying roughness function $h(x_o, y_o)$ and deformation $w(x_o, y_o)$ relative to the initially flat plane

$$E_o(x_o, y_o) = \exp(2ik\{h(x_o, y_o) + w(x_o, y_o)\}), \quad (7)$$

where the factor 2 appears due to the reflective configuration of the interferometer. After substituting for E_o and E_r in Eq. (6), the intensity distribution on the image plane becomes

$$I = E_i E_i^* = A_o^2 + A_r^2 + 2A_o A_r \cos[2k\{h(x_o, y_o) + w(x_o, y_o)\}], \quad (8)$$

where E_i^* is the complex conjugate of E_i . For a randomly rough object surface, $h(x_o, y_o)$ can be expressed statistically using probability density function $p(h)$. Among the available distribution forms, the most common one for random variations is the Gaussian distribution expressed in terms of rms roughness $\hat{\sigma}$ (Stover, 1995). A Gaussian surface height distribution with rms roughness $\hat{\sigma}$ has a probability distribution of the form

$$p(h) = \frac{1}{\hat{\sigma}\sqrt{2\pi}} \exp\left(-\frac{h^2}{2\hat{\sigma}^2}\right). \quad (9)$$

Then the ensembled average value of the intensity distribution over the illuminated area of the object is

$$\langle I \rangle = \int_{-\infty}^{\infty} p(h) I(h) dh = A_o^2 + A_r^2 + \frac{2A_o A_r}{\hat{\sigma}\sqrt{2\pi}} \int_{-\infty}^{\infty} \exp\left(-\frac{h^2}{2\hat{\sigma}^2}\right) \times \{\cos(2k\{h(x_o, y_o) + w(x_o, y_o)\})\} dh \quad (10)$$

where $\int_{-\infty}^{\infty} p(h) dh = 1$ has been used. Now, after expanding the cosine term in the above equation and simplifying, we get

$$\langle I \rangle = A_o^2 + A_r^2 + \frac{2A_o A_r \cos(2kw)}{\hat{\sigma}\sqrt{2\pi}} \times \int_{-\infty}^{\infty} \exp\left(-\frac{h^2}{2\hat{\sigma}^2}\right) \{\cos(2kh)\} dh - \frac{2A_o A_r \sin(2kw)}{\hat{\sigma}\sqrt{2\pi}} \times \int_{-\infty}^{\infty} \exp\left(-\frac{h^2}{2\hat{\sigma}^2}\right) \{\sin(2kh)\} dh = A_o^2 + A_r^2 + 2A_o A_r \exp(-2k^2 \hat{\sigma}^2) \cos(2kw(x_o, y_o)). \quad (11)$$

Equation (11) represents the intensity the interference fringes with maximas or minimas corresponding to the optical phase changes introduced by the out-of-plane deformation w . The result in Eq. (11) verifies the one obtained from an elementary analysis (Sinha and Tippur, 1997) wherein several implicit assumptions were made. The contrast of the interference fringes can now be expressed as

$$C = \frac{I_{\max} - I_{\min}}{I_{\max} + I_{\min}} = \frac{2A_o A_r}{A_o^2 + A_r^2} \exp(-2k^2 \hat{\sigma}^2). \quad (12)$$

Substituting for the wave number as $k = 2\pi/\lambda$, the fringe contrast can be expressed as a product of the contrast due to the surface roughness and the one due to the maximum amplitudes:

$$C = C_\alpha C_\sigma \quad \text{where}$$

$$C_\alpha = \frac{2A_o A_r}{A_o^2 + A_r^2} \quad \text{and} \quad C_\sigma = \exp\left(-\frac{8\pi^2 \hat{\sigma}^2}{\lambda^2}\right). \quad (13)$$

In the presence of a specularly reflective object surface, ($C_\sigma = 1$), the equations simplify to the classical equations of a Twyman-Green interferometer. The deformation $w(x_o, y_o)$ can be determined from constructive interference fringes by equating the argument of the cosine in Eq. (11) to $2N\pi$ where N is an integer. This leads to

$$w(x_o, y_o) = \frac{N\lambda}{2}, \quad (14)$$

where $N = 0, \pm 1, \pm 2, \dots$, represent the fringe orders. Thus, the light fringes occur for every $\lambda/2$ change in the optical path length and one could readily obtain a sensitivity of $\lambda/4$ ($\approx 2.65 \mu\text{m}$) by utilizing both dark and light fringes. From the interference analysis it is clearly evident that the roughness of the surface essentially influences the contrast of the fringes and the fringe interpretation is unaltered. Thus, the above analysis can be viewed as a more general field description with specular surfaces as a special case.

4 Measurement Limits on Rough Surfaces

Experiments to determine the ability of the interferometer in dealing with various degrees of random roughness were first carried out. A circular aluminum blank was manually polished using different fixed abrasives to vary surface roughness. (This method also represents the most common method of preparing surfaces for optical metrology.) Fixed abrasives of various commercially available grit sizes (#2000 (mean grit size = $1 \mu\text{m}$) to #60 (mean grit size = $250 \mu\text{m}$) emery paper) were used under dry conditions to alter the surface roughness. The resulting roughness $\hat{\sigma}$ was measured using a surface profilometer. The samples were then placed in the interferometer to obtain "wedge" fringes by applying a known rigid rotation about the horizontal axis resulting in an out-of-plane displacement of the form $w(x, y) \approx c_1 + c_2 y$, where c_i denote constants. Some representative fringes and the corresponding intensity distribution along the vertical diameter are shown in Fig. 4. These intensity profiles were subsequently analyzed to quantify average fringe contrast. The pixel intensity data along the vertical diameter over a narrow band were used in each case. A plot of normalized (with respect to an aluminum coated first surface mirror surface) fringe contrast as a function of the surface roughness parameter as well as grit size of the abrasive are shown in Figs. 5(a) and (b). Evidently, as the roughness of the surface increases, the fringe contrast deteriorates rapidly. The surface quality after polishing with #240 emery paper (mean abrasive grit size = $20 \mu\text{m}$) was found to provide a sufficiently high fringe contrast. Experiments reported here used #600 fixed abrasives to obtain fringe contrast in excess of 0.8.

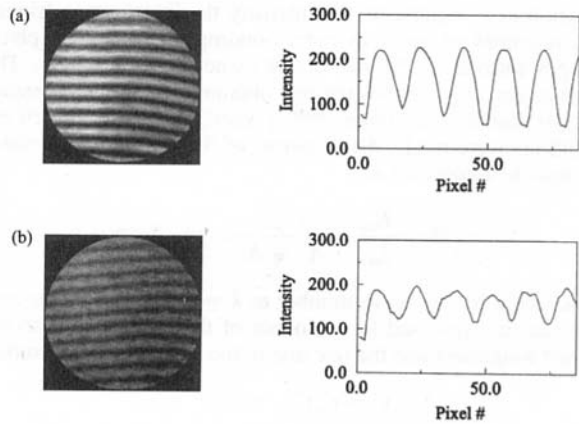


Fig. 4 Typical "wedge" fringes from the surfaces prepared using different grit size polishing papers (a) #600 (mean grit size 15 μm) (b) #60 (mean grit size 250 μm) and their corresponding intensity profile

5 Elastoplastic Crack-Tip Deformation Mapping

The ability of the interferometer to measure elastic deformations on rough surfaces has been demonstrated recently by the authors (Sinha and Tippur, 1997). In the following, crack-tip fields are mapped in homogeneous and bimaterial beams with little or no surface preparation to examine three-dimensional effects and J -dominance in the presence of substantial plastic deformations.

5.1 Homogeneous Cracked Beam. Aluminum (Al 6061-T6) beam samples were machined from a 6.25-mm rolled sheet of aluminum as obtained from the manufacturer. A through-the-thickness edge discontinuity of length (a) 6 mm and thickness (b) 150 μm was machined into the sample using a slitting saw. The specimen and its loading configuration ($L = 100$ mm, $W = 25$ mm) are shown in Fig. 6(a). In this case, the sample was used without any surface preparation (surface roughness 0.36 μm in the rolling direction and 0.34 μm in the transverse direction). It should be noted that this roughness ($\delta/\lambda \approx 0.03$) yields sufficiently high fringe contrast without any surface preparation. The specimen was subjected to symmetric three-point bending in a displacement-controlled loading device. A 0.3-mm diameter pencil lead (commonly used in mechanical pencils) was temporarily attached to the sample surface to obtain a sharp focus of the crack-tip region. The crack-tip deformations were mapped using the interferometer in real-time. Some representative interference patterns of contours of constant $w(x, y)$ fringes near the crack tip for different load levels are shown in Fig. 6(b) and (c). Knowing the nominal thickness B of the beam, the average out-of-plane strain ϵ_z ($\approx 2w(x, y)/B$) can be estimated from the fringes. In Fig. 6(c) crack-tip fringes represent a strain ϵ_z of approximately 0.02 while the outermost fringe corresponds to 0.0045. It should be noted that these values represent strain values beyond the yield strain ϵ_0 (≈ 0.0038) for Al 6061-T6. Further, it will be shown later that the Dugdale plastic zone estimate (r_p) in this case is approximately 1.8 B while the one shown in Fig. 1 is only 0.6 B for the same material. As discussed earlier, the permanent deformations near the crack tip alter the surface texture and increase the local roughness and affects the fringe visibility when visible light is used. However, the discernability and contrast of the fringes near the crack-tip region are rather excellent in Fig. 6 with the use of infrared wavelength.

To obtain an estimate of the size of the zone of dominant three-dimensional deformations near the crack tip, a complementary elastoplastic plane-stress finite element analysis based on the incremental theory of plasticity and the J_2 -flow rule was carried out using ANSYS software package. The finite element model consisted of 1728 eight-node plane-stress quadrilateral

elements and 5377 nodes. No singular elements were embedded at the crack tip. The crack-tip region was discretized using a fine mesh with 576 crack-tip elements within a radius of $r/B = 1$ and 1440 elements within $r/B = 2$ from the crack tip. It was ensured that finite element discretization was adequate to satisfactorily capture the full-field singular behavior near the crack tip and the results have been reported elsewhere (Sinha et al., 1997). The stress-strain relations necessary for the elastoplastic simulations were based on a uniaxial material model

$$\begin{aligned} \left(\frac{\epsilon}{\epsilon_0}\right) &= \left(\frac{\sigma}{\sigma_0}\right) \quad \text{for } (\sigma \leq \sigma_0) \\ \left(\frac{\epsilon}{\epsilon_0}\right) &= \alpha \left(\frac{\sigma}{\sigma_0}\right)^m \quad \text{for } (\sigma > \sigma_0). \end{aligned} \quad (15)$$

In the above, ϵ_0 , σ_0 are yield strain and stress, m is the hardening index, and α is a constant. For Al 6061-T6, values of $m = 18$ and $\alpha = 1.22$, were used (Chiang et al., 1988). The model was subjected to three-point bending similar to the experiments. Using material incompressibility, out-of-plane displacements can be computed around the crack tip using

$$\epsilon_z^p = -(\epsilon_x^p + \epsilon_y^p) \approx -\frac{2w}{B}, \quad (16)$$

where the superscript "p" denotes plastic component. The measured and computed values of out-of-plane displacements are plotted in Fig. 7 for $P/P_0 = 1.04$ along several discrete directions θ ahead of the crack tip. Here the out-of-plane displacements and radial distances are normalized by the initial notch width b and specimen thickness B , respectively. In each of these plots, the region of disagreement between the two data sets by more than ten percent is identified as a region of dominant three-dimensional effects. Generally, three-dimensional deformations seem to dominate within $r/B \approx 0.35$, when $67.5 \text{ deg} < \theta < 67.5 \text{ deg}$. (In the regions beyond this value of θ , the optical information is rather limited and direct comparison was not carried out.) Beyond this region, plane-stress behavior

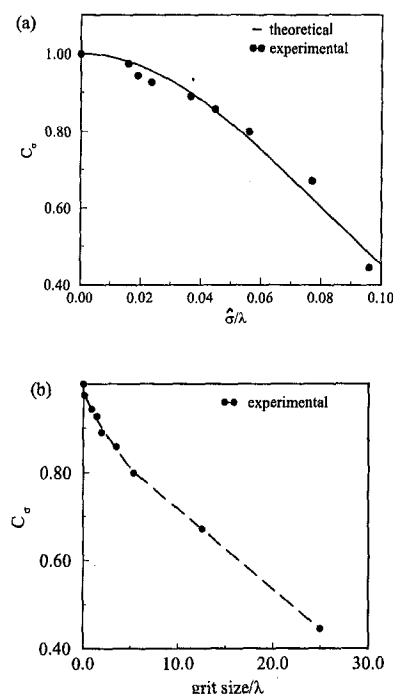


Fig. 5 Plot of fringe contrast as a function of (a) surface roughness (b) grit size

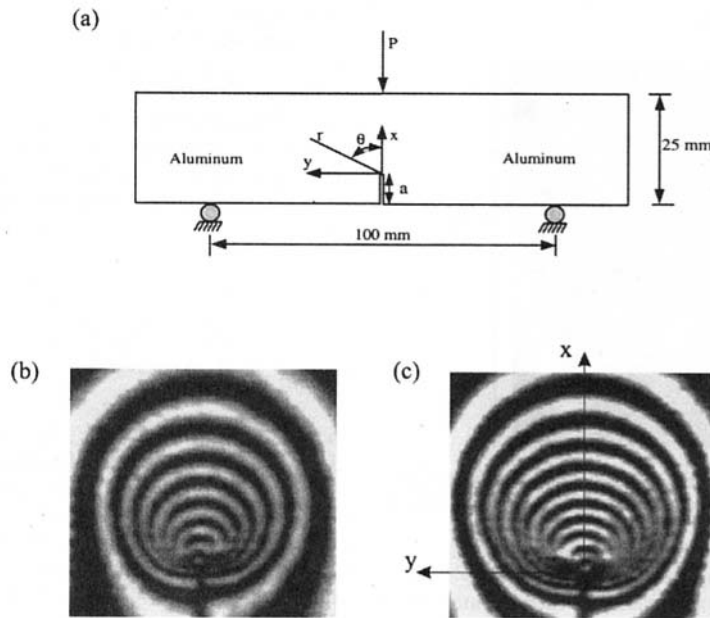


Fig. 6 Homogeneous three-point bending experiments: (a) loading configuration, (b) and (c) interference patterns representing contours of $w(x, y)$ fringes near the crack tip for $P/P_0 = 0.98$ and 1.04 , respectively

is evident. The size of the three-dimensional zone seen here is generally comparable to the ones reported in the literature. A three-dimensional zone of size $r/B \cong 0.5$ is reported by Zehnder and Rosakis (1990) in three-point bend samples in steel samples with EDM cut notches using caustics and interferometry. A somewhat larger three-dimensional zone of size $0.8-1.0B$ is

observed by Chiang and Hareesh (1988) in aluminum tensile sheets with extensive plasticity near fatigue cracks using geometric moiré methods and a more stringent error band of 2.5 percent. Crack tunneling on the midplane of the sheet and lower measurement sensitivity are other possible explanations for the difference.

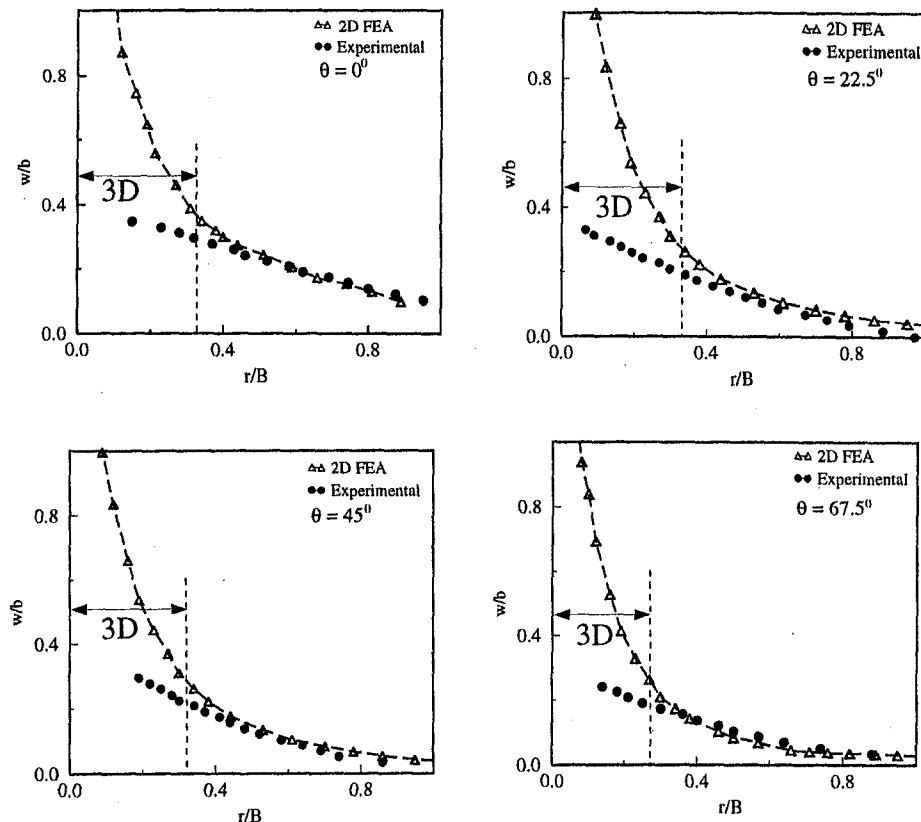


Fig. 7 Variation of out-of-plane displacements from the measurements and two-dimensional plane-stress simulations along different directions for the aluminum beam

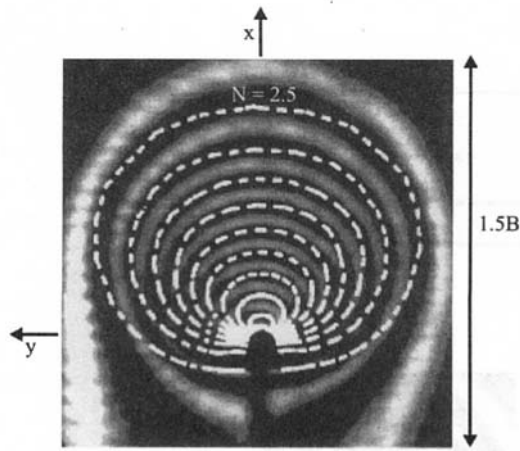


Fig. 8 Superposition of finite element contours (broken lines) from a three-dimensional simulation over the interferometric fringes for the aluminum beam

To ensure that the differences between the measurements and two-dimensional simulations are indeed due to three-dimensional effects, an elastoplastic three-dimensional finite element analysis was carried out. Four layers of eight-node (three-degree-of-freedom/node) brick elements were used in the model which consisted of 4000 elements and 5226 nodes. The contours of constant out-of-plane displacement were computed on the surface. A direct superposition of the experimental fringes and the finite element contours (broken lines) around the crack tip is shown in Fig. 8. A good agreement between the two results is readily evident even in the regions very close to the crack tip previously identified as regions of dominant three-dimensional effects. In Fig. 9(a), a representative plot of the measurements along with the ones from two-dimensional and three-dimen-

sional simulations are shown for $\theta = 22.5$ deg and good agreement between measurements and three-dimensional simulation clearly becomes evident.

The J -integral is the fracture parameter which describes the strain amplification near a ductile crack tip (Rice, 1968). The optical measurements can be used to directly calculate the J -integral using the so-called HRR equation (Hutchinson, 1968; Rice and Rosengren, 1968) for out-of-plane strain

$$\begin{aligned} \epsilon_z^p &\approx -\frac{2w}{B} \\ &= -\frac{\alpha\sigma_o}{E} \left(\frac{EJ}{\alpha\sigma_o^2 I_m r} \right)^{m/(m+1)} [\hat{\epsilon}_r(\theta; m) + \hat{\epsilon}_\theta(\theta; m)]. \end{aligned} \quad (17)$$

In the above, functions $\hat{\epsilon}_r$, $\hat{\epsilon}_\theta$, and I_m are tabulated by Shih (1983) for known values of material hardening index m . Now, using Eqs. (17) and (14), the value of the J -integral for different fringe orders are evaluated and are plotted as a function of r/B in Fig. 9(b). Evidently, the value of the J -integral outside the region of three-dimensional deformations remains relatively constant over $0.35 < r/B < 0.65$ (shaded region) and can be identified as the region of J -dominance. As one moves farther away from the crack tip ($r/B > 0.65$), the far-field effects become significant and the evaluated values of the J -integral are no longer constant.

The value of the J -integral can also be estimated independently as $J = J_e + J_p$, where J_e is computed from the elastic stress intensity factor using an effective crack length. Consider the plane-stress condition

$$J_e = \frac{K_I^2(a_e)}{E}, \quad (18)$$

where

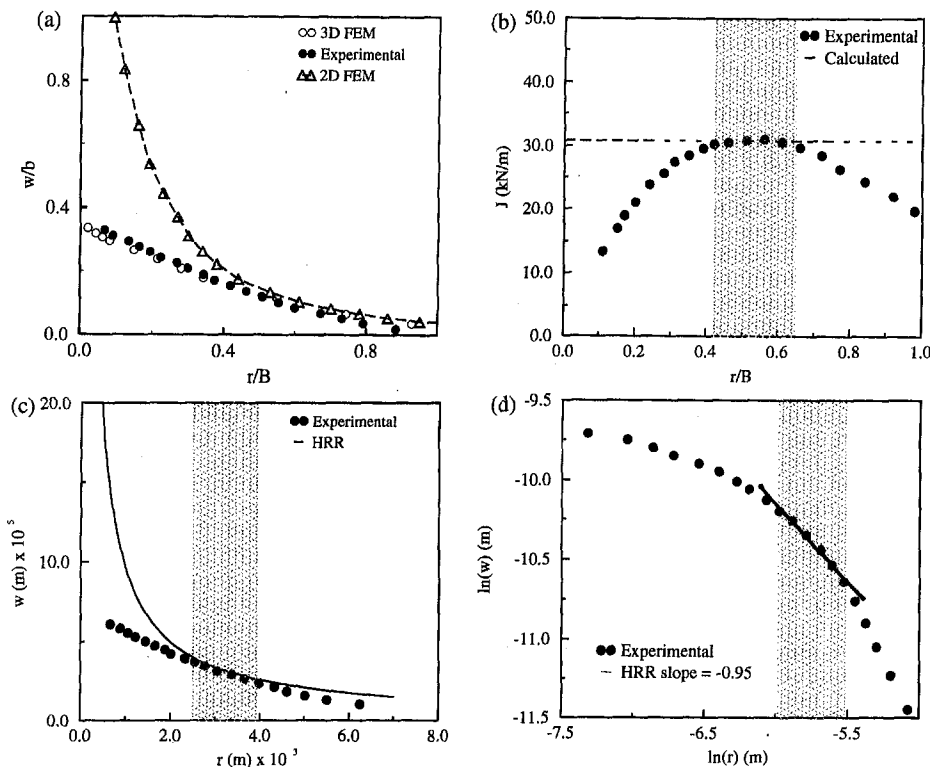


Fig. 9 Crack-tip three-dimensionality and J -dominance in aluminum beams ($\theta = 22.5$ deg); (a) plot of normalized displacements with normalized distance, (b) computed and measured values of the J -integral with normalized distance, (c), (d) comparison of optical measurements with HRR-prediction

$$a_e = a + \frac{1}{1 + \left(\frac{P}{P_o}\right)^2} \frac{1}{2\pi} \left(\frac{m-1}{m+1}\right) \left(\frac{K_I(a)}{\sigma_o}\right)^2.$$

Now

$$K_I = \frac{P}{B\sqrt{W}} f\left(\frac{a}{W}\right), \quad \text{where } f\left(\frac{a}{W}\right)$$

is a nondimensional function of the ratio a/W . The effective crack length (a_e) is evaluated iteratively until convergence is achieved. The value of J_p is estimated using

$$J_p = \alpha \epsilon_o \sigma_o (W - a) h_1 \left(\frac{P}{P_o}\right)^{m+1}, \quad (19)$$

where $P_o (= (1.072B(W - a)^2 \sigma_o)/L)$ is a reference load corresponding to a fully plastic ligament under plane-stress conditions. A detailed tabulation of the function $h_1(a/W)$ can be found in Kumar et al. (1981). From the above, the calculated value of the J -integral was found to be 30.8 kN/m and is in good agreement with the measured values of the J -integral in the shaded region of Fig. 9(b). Outside this region, ($0 < r/B < 0.35$ and $r/B > 0.65$) the J -integral is underestimated by the measurements.

The measured out-of-plane displacements are finite at the crack tip unlike the HRR predictions based on two-dimensional assumptions. The out-of-plane displacements based on HRR prediction and the measured value of the J -integral is plotted in Fig. 9(c) (solid line). The predictions and measurements deviate substantially very close to the crack tip while the agreement is rather good in the region $0.35 < r/B < 0.65$ (shaded region). Based on the measured value of the J -integral, one can get a Dugdale plastic zone estimate $r_p = (\pi/8)(JE/\sigma_o^2) \cong 1.8B$ for this load level. Previous studies (Zehnder and Rosakis, 1990) have shown that the HRR region exists within $r = 0.3r_p$. The shaded region indeed corresponds to such a prediction with three-dimensional region acting as the inner limit of the zone of J -dominance. From Eq. (17) it can be seen that the slope of $\log(w)$ versus $\log(r)$ plot should be $-(m/(m+1))$ (≈ -0.95 for Al 6061-T6) for HRR field to prevail. The data points corresponding to the shaded region in Fig. 9(c) indeed reflect the expected slope in Fig. 9(d) suggesting a J -dominant behavior over this distance.

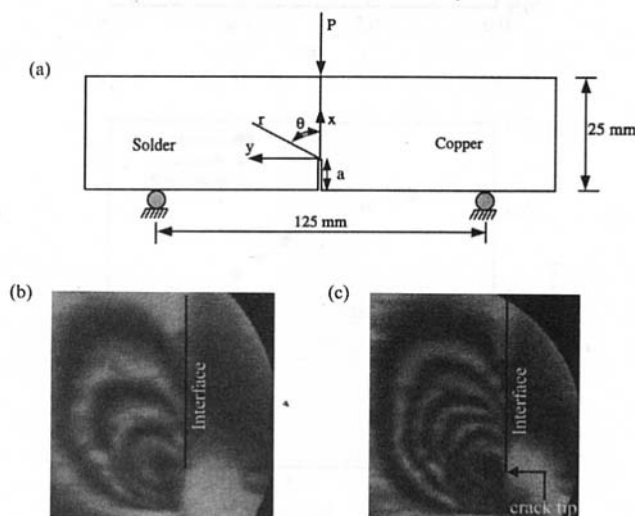


Fig. 10 Bimaterial three-point bending experiments; (a) loading configuration, (b) and (c) interference patterns representing contours of $w(x, y)$ fringes near the crack tip for $P/P_o = 1.57$ and 1.65 , respectively

Table 1 Material properties of the bimaterial samples

Material	E (GPa)	ν	σ_o (MPa)	m	α
63/37 solder	20	0.4	20	11	1
Copper	124	0.33	70	—	—

5.2 Solder-Copper Bimaterial Beam With an Interfacial Crack.

At the moment, optical investigation of deformation fields near elastoplastically deformed interfacial cracks is lacking. The method of infrared Twyman-Green interferometry is next extended to map out-of-plane displacements near elastoplastic interfacial cracks. Solder-copper bimaterials, which have a great deal of significance to the electronic industry, are examined using the new optical technique. The solder used in the investigation was obtained from 63/37 Sn-Pb solder ingots. Bimaterial samples ($150 \times 25 \times 5$ mm) with edge cracks ($a/W = 0.25$) were prepared by joining solder and copper bars (see Fig. 10(a)) in a specially designed aluminum fixture. An edge crack was introduced between the solder and copper bars during the bonding process. Soldering flux (Kester 185, type RMA) was applied to the edges of the bars where bonding was needed and was allowed to stay until the flux became tacky. The fixture was heated until the solder started melting. The bonded sample was then cooled to room temperature in air and subsequently machined to the final dimensions. The resulting bimaterial had interfacial cracks of thickness less than $50 \mu\text{m}$. The surface preparation consisted of simply polishing the surface using #600 grit fixed abrasive. The beam samples were subjected to symmetric three-point bending with the loading point located < 1 mm away from the interface on the copper side. A monotonically increasing load (strain rate in solder $\dot{\epsilon} \approx 10^{-4} \text{ sec}^{-1}$, Krishnamoorthy and Tippur, 1998) was applied to the sample in a displacement controlled loading device and the crack-tip deformations were measured in real-time. Typical interference patterns representing contours of constant $w(x, y)$ are shown in Figs. 10(b) and (c) for two load levels $P/P_o = 1.57$ and 1.65 . Here reference load P_o was calculated based on the yield stress of solder (see, Table 1). It is clearly evident that the deformations primarily occur on the solder side of the bimaterial and the ones on the copper side are negligible. Further, the deformations on the solder side of the bimaterial represent strain levels beyond the yield strain ϵ_o of solder (≈ 0.001) in the entire region of observation. That is, the smallest measurable fringe order $N \approx 0.5$ denotes a strain component ϵ_z approximately equal to ϵ_o .

To obtain an estimate of the size of the zone of dominant three-dimensional deformations near the crack tip, a complementary elastoplastic plane-stress finite element analysis was carried out similar to the ones reported in the Section 5.1. The 63/37 solder is a relatively low-yield strength nonlinear material. Hence, permanent deformations mainly occur on the solder side of the bimaterial and the situation is similar to an elastoplastic material on the rigid substrate. Here, the solder is modeled as a power-law hardening material ($\epsilon/\epsilon_o = \alpha(\sigma/\sigma_o)^m$ (for $\sigma > \sigma_o$)) using the uniaxial test data reported by Skipor et al. (1996) for a strain rate of $\dot{\epsilon} \approx 10^{-4} \text{ sec}^{-1}$. The data were fitted with a power-law equation and the resulting parameters along with other relevant mechanical properties are shown in Table 1.

The model was subjected to three-point bending as in the experiments and the values of $w(x, y)$ were computed in the solder half using material incompressibility condition. To estimate the region of plane-stress behavior on the solder side, out-of-plane displacements are plotted against r/B along a few discrete directions θ in Fig. 11. In these plots the region with disagreement exceeding ten percent between the two data sets near the crack tip is identified as the region where the three-dimensional effects are dominant. The plots also suggest that a plane-stress assumption is reasonable beyond $r/B \approx 0.5$ and 30

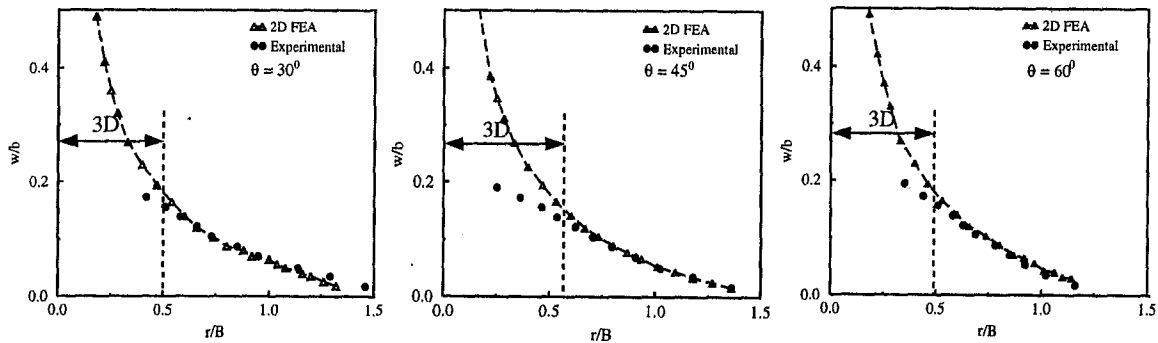


Fig. 11 Variation of out-of-plane displacements from the measurements and two-dimensional plane-stress simulations along different directions for the solder-copper bimaterial beam

deg $\leq \theta \leq 60$ deg. It should be noted that the optical data along other directions beyond $\theta = 60$ deg are rather limited for performing direct comparison. Here, we also need to recognize that three-dimensional effects dominate all along the interface ($0 < \theta < 30$ deg) and elastic counterpart investigations are reported by Lee and Rosakis (1993) and Sinha, et al. (1997).

To confirm that the disagreements in Fig. 11 are primarily due to the three-dimensional effects, an elastoplastic three-dimensional finite element analysis was carried out. The model is similar to the one described in the previous section. The contours of out-of-plane displacement $w(x, y)$ were generated from the computed results on the surface of the model. A direct superposition of experimental and finite element contours (broken lines) is shown in Fig. 12. A good agreement between the two is observed even very close to the crack tip. This is further demonstrated in Fig. 13(a) where normalized displacements from the experiments and two-dimensional and three-dimensional elastoplastic simulations are plotted against (r/B) for $\theta = 45$ deg for an applied load level of P/P_0 equal to 1.65. Unlike the two-dimensional finite element results, the three-dimensional computations suggest a finite value of out-of-plane displacement at the crack tip. Moreover, the computed value of $w(x, y)$ at the crack tip is lower than the one at a small distance ahead of the crack tip and along the interface. It should be recognized that the copper half undergoes negligible out-of-plane deformation and hence copper can be viewed as a rigid

substrate relative to solder. This in turn implies that the out-of-plane displacements along $(x \geq 0, y = 0)$ are zero and correspondingly the simulations show a down turn in the out-of-plane displacement value as the crack tip is approached. The two-dimensional finite element results, however, deviate substantially from the experiments in the near vicinity of the crack predicting a singular behavior.

Although at the moment there are no explicit closed-form field solutions for a plastically deformed interfacial crack-tip region, there is evidence suggesting that for tensile dominated (or, "opening" dominated) loading, the stresses and strains are scaled by the J -integral (Shih, 1991) and bear striking resemblance to mixed-mode HRR-like fields in homogeneous media. The following form of the dominant term is suggested for strain components near an elastoplastic interfacial crack:

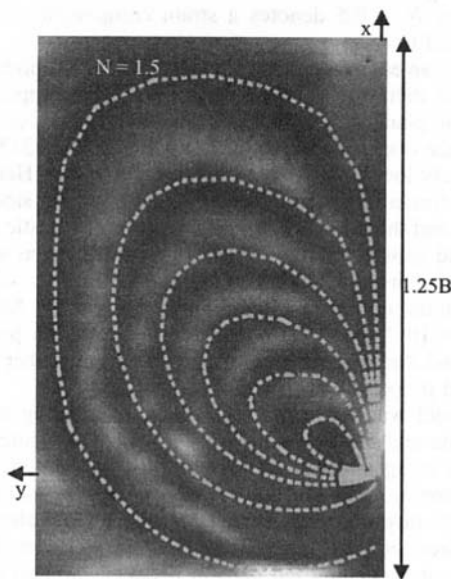


Fig. 12 Superposition of finite element contours (broken lines) from a three-dimensional simulation over the interferometric fringes for the solder-copper bimaterial beam

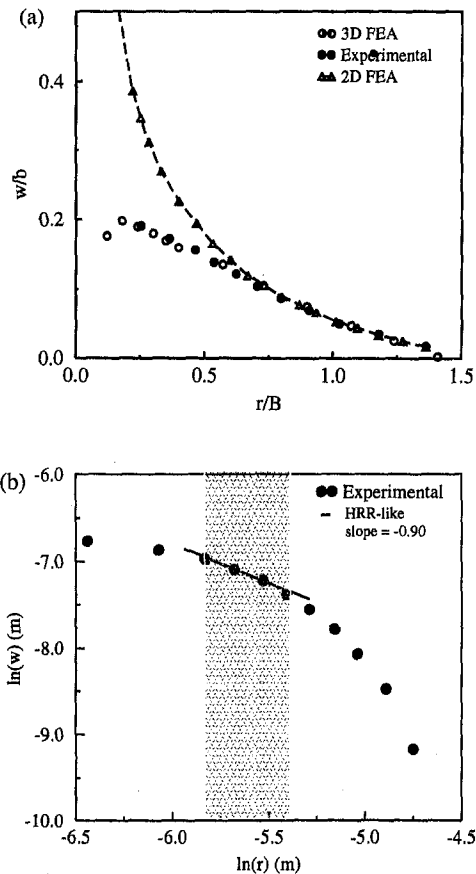


Fig. 13 Crack-tip three-dimensionality and J -dominance in solder-copper bimaterial beams ($\theta = 45$ deg); (a) plot of out-of-plane displacements, (b) comparison of optical measurements with HRR-prediction

$$\epsilon_{ij} = \alpha \epsilon_o \left(\frac{J}{\alpha \epsilon_o \sigma_o I_m r} \right)^{m/(m+1)} \hat{\epsilon}_{ij}(\theta, \hat{r}, \xi, m), \quad (20)$$

where $\hat{\epsilon}_{ij}$ is a slowly varying function of \hat{r} ($=r\sigma_o/J$) and ξ is the so-called plastic mode mixity. In Eq. (20), σ_o , ϵ_o represent the yield stress and strain of the softer of the two materials. The above are deductions based on numerical simulation and direct experimental evidence of the same is currently lacking. In view of this, the experimental data is examined for evidence of a HRR-like behavior. In Fig. 13(b), $\log(w)$ is plotted against $\log(r)$ for the solder-copper interface. Knowing the hardening index m for 63/37 solder, when $\log(w)$ is plotted against $\log(r)$, a slope of $-(m/(m+1))$ (≈ -0.9) should be recoverable if a HRR-like field were to prevail in the crack-tip vicinity. In Fig. 13(b), such a behavior indeed is seen over $0.5 < r/B < 0.75$ (shaded region) and suggests J -dominance over this distance.

6 Conclusions

A novel infrared interferometer using 10.6- μm coherent infrared radiation has been developed for performing real-time full-field measurements on rough surfaces. A rigorous Fourier optics analysis that uses Fresnel diffraction principle and a Gaussian surface roughness profile is provided. The infrared interferometer is shown to be an effective tool for elastoplastic crack-tip field investigation in ductile solids. The range of surface roughness over which measurements can be effectively made is experimentally demonstrated. Fringe contrast in excess of 0.5 can be realized with surfaces with roughness parameter $\hat{\sigma} = 0.8 \mu\text{m}$ (or, $\hat{\sigma}/\lambda \approx 0.08$) while fringe contrast in excess of 0.8 can be obtained with roughness of $\hat{\sigma} = 0.35 \mu\text{m}$ (or, $\hat{\sigma}/\lambda \approx 0.03$). In fact, the latter is shown to be easily achievable simply by polishing the sample surface with a #600 (mean grit size 15 μm) fixed abrasive. The proposed interferometer bridges the sensitivity gap between the visible light Twyman-Green interferometer (submicron sensitivity) and shadow/projection moiré methods (25–50 $\mu\text{m}/\text{fringe}$) used for mapping out-of-plane deformations.

The region of three-dimensional deformations near elastoplastically deformed cracks in homogeneous and bimaterial beams are examined. The measurements are investigated along with companion two-dimensional and three-dimensional elastoplastic finite element simulations. In the beam configurations studied, three-dimensional effects dominate within $r/B = 0.35$ while plane-stress conditions exist beyond this region in homogeneous specimens. The optical measurements have been used to directly quantify the J -integral and the HRR predictions agree with the experiments over $0.35 < r/B < 0.65$. Experimental measurement of elastoplastic deformations near interfacial cracks are reported for solder-copper bimaterials. In the region $y > 0$, three-dimensional deformations seem to dominate over $r/B \leq 0.5$ and along the interface. In the absence of explicit elastoplastic interfacial crack-tip solutions, the existence of a region of a HRR-like deformation field is investigated and found to prevail over $0.5 \leq r/B \leq 0.75$ ahead of the crack.

Acknowledgments

Some of the equipment used in this research were acquired through NSF grant CMS9313153. Support for studying solder-copper interfaces were through AFoSR grant AF-F49620-97-10167.

References

- Beckmann, P., and Spizzichino, A., 1963, *The Scattering of Electromagnetic Waves from Rough Surfaces*, Pergamon Press, New York.
- Chiang, F. P., and Hareesh, T. V., 1988, "Three dimensional crack tip deformations: An experimental study and comparison to HRR field," *International Journal of Fracture*, Vol. 36, pp. 243–257.
- Chiang, F. P., Hareesh, T. V., Liu, B. C., and Li, S., 1988, "Optical Analysis of HRR Field," *Optical Engineering*, Vol. 27, pp. 625–629.
- Hutchinson, J. W., 1968, "Singular behavior at the end of a tensile crack tip in a hardening material," *Journal of the Mechanics and Physics of Solids*, Vol. 16, pp. 13–31.
- Iizuka, K., 1985, *Engineering Optics*, 2nd Ed., Springer-Verlag, New York.
- Krishnamoorthy, H., and Tippur, H. V., 1998, "Evaluation of Elasto-Plastic Interfacial Fracture Parameters in Solder-Copper Bimaterial Using Moiré Interferometry," *ASME Journal of Electronic Packaging*, Vol. 120, pp. 267–274.
- Kumar, V., German, M. D., and Shih, C. F., 1981 "An engineering approach for elastic-plastic fracture analysis," EPRI Report NP-1931, Electric Power Research Institute, Palo Alto, CA.
- Kwon, O., Wyant, J. C., and Hayslett, C. R., 1980, "Rough surface interferometry at 10.6 μm ," *Applied Optics*, Vol. 19, pp. 1862–1869.
- Lee, Y. J., and Rosakis, A. J., 1993, "Interfacial crack in plates: A three-dimensional numerical investigation," *International Journal of Solids & Structures*, Vol. 30, pp. 3139–3158.
- Lewandowski, J., 1989 "Lateral shear interferometer for infrared and visible light," *Applied Optics*, Vol. 28, pp. 2373–2379.
- Munneryn, C. R., and Latta, M., 1968, "Rough surface interferometry using CO₂ laser source," *Applied Optics*, Vol. 7, pp. 1858–1859.
- Persson, U., 1993 "Roughness measurement of machined surfaces by means of the speckle technique in the visible and infrared regions," *Optical Engineering*, Vol. 32, pp. 3327–3332.
- Rice, J. R., 1968 "A Path-Independent Integral and the Approximate Analysis of Strain Concentration by Notches and Cracks," *ASME JOURNAL OF APPLIED MECHANICS*, Vol. 35, pp. 379–386.
- Rice, J. R., and Rosengren, G. F., 1968, "Plane strain deformation near a crack tip in a power law hardening material," *Journal of the Mechanics and Physics of Solids*, Vol. 16, pp. 1–12.
- Shih, C. F., 1983, "Tables of Hutchinson-Rice-Rosengren Singular Fields Quantities," Materials Research Laboratory, Brown University, Providence, RI.
- Shih, C. F., 1991, "Cracks in bimaterial interfaces: Elasticity and plasticity aspects," *Materials Science and Engineering*, Vol. A143, pp. 77–90.
- Sinha, J. K., Tippur, H. V., and Xu, L., 1997, "An interferometric and finite element study of interfacial crack tip fields and the influence of mode-mixity on 3-D deformations," *International Journal of Solids and Structures*, Vol. 34, pp. 741–754.
- Sinha, J. K., and Tippur, H. V., 1997 "Infrared Interferometry for rough surface measurements: Application to failure characterization and flaw detection," *Optical Engineering*, Vol. 36, No. 8, pp. 2233–2239.
- Skipor, A. F., Harren, S. V., and Botsis, J., 1996, "On the Constitutive Response of 63/37 Sn/Pb Eutectic Solder," *ASME Journal of Engineering Materials and Technology*, Vol. 118, pp. 1–11.
- Stover, J. C., 1995, *Optical Scattering*, SPIE Press, Bellingham, WA.
- Timoshenko, S. P., and Goodier, J. N., 1970, *Theory of Elasticity*, 3rd Ed., McGraw-Hill, New York.
- Tippur, H. V., S. Krishnaswamy, and Rosakis, A. J., 1991 "Optical Mapping of Crack Tip Deformations using the Methods of Transmission and Reflection Coherent Gradient Sensing: A Study of Crack Tip K -dominance," *International Journal of Fracture*, Vol. 52, pp. 91–117.
- Zehnder, A. T., and Rosakis, A. J., 1990 "Three-Dimensional Effects Near a Crack Tip in a Ductile Three-Point Bend Specimen, Part II: An Experimental Investigation Using Interferometry and Caustics," *ASME JOURNAL OF APPLIED MECHANICS*, Vol. 57, pp. 618–626.